Aerodynamic Design and Analysis of a Formula SAE Drag Reduction System (DRS)

Conference Paper · April 2020

DOI: 10.4271/2020-01-0685

1 author:

David Penner
University of Manitoba
1 PUBLICATION **0** CITATIONS

SEE PROFILE

2020-01-0685 Published 14 Apr 2020

Aerodynamic Design and Analysis of a Formula SAE Drag Reduction System (DRS)

David J. Penner University of Manitoba

Citation: Penner, D.J., "Aerodynamic Design and Analysis of a Formula SAE Drag Reduction System (DRS)," SAE Technical Paper 2020-01-0685, 2020, doi:10.4271/2020-01-0685.

Abstract

Formula SAE vehicles, like many other vehicles within motorsport, often employ rear mounted aerodynamic devices to improve cornering performance, these devices can however have a significant amount of aerodynamic drag. Additional speed can be gained by reducing the impact of the rear wing on the straightaways of the track through the use the aptly named Drag Reduction System (DRS), which works by reducing the angle of attack of the rear wing flap(s).

A DRS can however introduce other performance losses, including the losses from having a gap between the rear wing flaps and endplate to prevent friction, the potential to stall the rear wing from improper opening angles of the flaps, and from the wake of the DRS actuator if positioned in front of the airfoils. An additional concern is the time it takes for the rear wing performance to return upon DRS deactivation, which will affect how long before corner entry the driver must disable the system.

Insight into each of these problems as well as the optimum opening angles was found through the use of CFD using Siemens' STAR-CCM+ 2019.1. Simplified geometry came from UMSAE Polar Bear Racing's car, PBR20, out of the University of Manitoba. All steady state simulations were done using RANS, while the DRS deactivation study was done using a novel method using Detached Eddy Simulation (DES), where dynamic overset meshes were used to model the transient motion of the flaps. As a result of the deactivation study, new insight was gained into the dynamic behaviour of drag reduction systems.

Introduction

Formula SAE

Formula SAE is one of the several competitions that is a part of SAE International's Collegiate Design Series (CDS). These competitions allow post secondary students across the world to gain hands on engineering experience by creating small prototype vehicles designed for specified tasks. In the case of Formula SAE it is to create an open wheeled racecar to be raced on autocross courses. While these cars are limited in speed through regulations that restrict their power, the design of the race courses heavily rewards cornering ability. As a result, a primary emphasis on development is on cornering ability, resulting in some teams creating cars being able to corner at rates of over 2 [g].

Due to the combination of the relatively low speeds of the cars (averaging 50 [*kph*]) and the high emphasis on cornering ability, the current state of the art for these competitions has evolved to include the use of extreme, high downforce (negative lift) producing aerodynamic devices. Since the aerodynamics of these cars are designed with a low emphasis on aerodynamic efficiency, aerodynamic drag coefficients in the range of C_D = 1.0-1.5 are common. While this drag is acceptable given the performance gained due to increased grip from downforce, the race tracks in Formula SAE will all include straightaway sections that reward cars with lower drag.

Drag Reduction System (DRS)

The problem of unnecessary drag on straightaways resulting from downforce producing aerodynamic components is not a new problem in the world of motorsports. In 2011, Formula 1 teams began implementing a Drag Reduction System (DRS) to their car, reducing the angle of attack of their rear wing flap in order to reduce drag on predetermined zones of the track. Since then, Formula SAE teams have began to implement a DRS on their car for the same reason. These systems can have aerodynamic drawbacks depending on their implementation, which could result in reduced performance not only because of the activation of the DRS, but also when the system is not active. These losses will be herein referred to as 'active' and 'passive' losses respectively.

Active losses can be split into two effects, the loss in downforce and flow structure of the rear wing due to the opening of the flaps, and the time it takes for the downforce to return once the flaps close. Depending on the design of the rear wing there exists a potential for the main plane of the rear wing to stall upon DRS activation, which could result in

a larger response time of the rear wings donwnforce upon DRS deactivation due to the larger change in flow structure. The second effect is that a stalled wing would create an even further reduction in downforce, which while not important for speed in a straight line, would reduce the aerodynamic stability of the car in a time where the car will be at its maximum speeds. The second loss due to the activation of the DRS is due to the systems behaviour upon its deactivation. The return profile of downforce upon deactivation of the DRS is not well studied, with an initial attempt being made with aeroelastic modelling [1]. This unknown dynamic behaviour is further complicated by the variety of different DRS implementations throughout Formula SAE.

The existence of passive losses varies depending on the implementation of the DRS, specifically the positioning of the actuator and mechanical linkages, as well as the gap required between the flaps and endplate of the rear wing to prevent binding during activation. Positioning of the actuation mechanism can vary, with some teams using a servo motor inside of their airfoils connected to kinematic linkages on external side of the endplates, and other teams using a pneumatic cylinder mounted directly to the main plane of the rear wing connected to the flaps with linkages, all directly in the path of the air flowing into the flaps. Losses due to the gap between the endplates and the flaps are less a matter of design choices, but rather due to manufacturing tolerances. This gap would affect the performance of the wing by reducing the effect of the endplate on the flaps, allowing some air to leak from the high pressure side of the flaps to the low pressure side.

Computational Fluid Dynamics

In the modern age of aerodynamics, the majority of initial development is done through the use of computational fluid dynamics (CFD) as it allows for low cost concept exploration and design refinement. This is especially true for student competitions such as Formula SAE as many universities lack facilities such as wind tunnels, let alone full-scale automotive wind tunnels with rolling roads. This has lead many Formula SAE teams to go through their entire design process using aerodynamic simulation, leaving physical testing for validation work of the completed car.

Research Aim

The purpose of this work is to:

- Determine the effect of flap opening angle combinations on downforce, drag, aerodynamic efficiency, and aerodynamic balance
- Gain insight into the aerodynamic behaviour of a DRS being closed
- Determine the effect of the flap-endplate gap size on wing performance
- Determine the aerodynamic losses from the DRS actuator wake

Computational Setup

Two different computational setups will be used for our analysis, with a RANS setup being used for every simulation except for the DRS deactivation simulation which used a Detached Eddy Simulation. Each simulation was performed using STAR-CCM+ 2019.1 (Build 14.02.010). The geometry used for all simulations was a simplified, CFD ready version of the PBR20 vehicle from the University of Manitoba Student Chapter of SAE International's Formula SAE team, UMSAE Polar Bear Racing.

All simulations originated from the same car model and domain sizing as shown in figures 1 and 2, each using a symmetry condition down the centerline of the car in order to reduce computational cost. The inlet face of the domain was placed 5L forward of the front of the car, where L=3.0 [*m*] is the length of the car. The freestream velocity was 20 [*m/s*] with a turbulent viscosity ratio of 200 and a turbulent intensity of 1%. The top and side faces of the domain are 5H (H=1.2 [*m*]) and 5W (W=1.4 [*m*]) away from the car respectively, each with slip conditions applied such that the velocity gradient near the wall was zero. The domain outlet was 10L behind than the rear of the car, set to a pressure outlet condition. The ground for the simulation was modelled as a moving road with the speed being set to match the freestream velocity of the simulation, the wheel surfaces also have the appropriate tangential velocity applied to them to match the road velocity.

Meshing best practices are taken from Siemens' webinar *Online Formula Student Training* [2], giving recommendations on a series of volumetric refinements and prism layer properties. Using a base size of 20 [*mm*], this resulted in an underbody refinement to 10 [*mm*], a large box around the vehicle

FIGURE 1 UMSAE PBR20

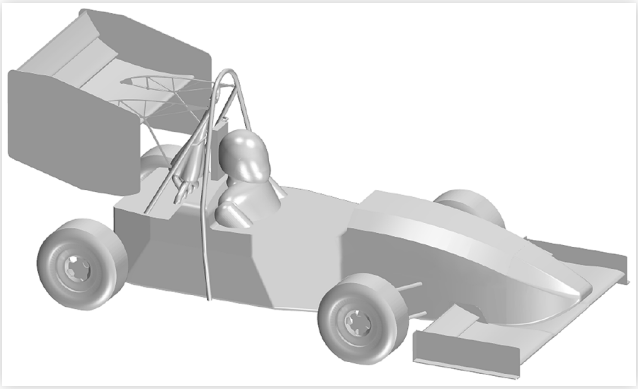

FIGURE 2 Computational domain

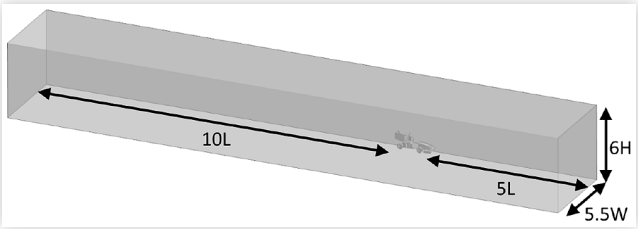

FIGURE 3 Volumetric refinements

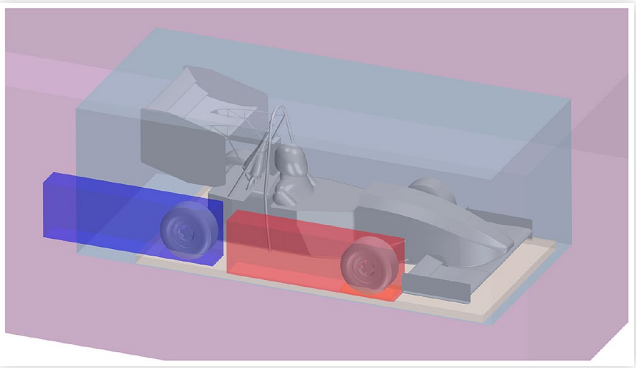

extending upwards, forwards, and to the side by 1 [*m*], and rearwards to the end of the domain with a with a mesh sizing of 80 [*mm*], a more constrained wake around the car and 1.5 [*m*] rearward refined to 20 [*mm*], tire wake refinements extending 1 [*m*] rearward to 10 [*mm*], and tire contact patch refinements to 2.5 [*mm*]. In order to achieve a wall y+<1 on all airfoils, 24 layers were generated with a near wall thickness of 0.021 [*mm*], and a total prism layer thickness of 8.0 [*mm*]. All other surfaces were meshed to achieve y+<5, the rest of the car received 13 layers with a near wall thickness of 0.082 [*mm*], and a total prism layer thickness of 8.0 [*mm*], the ground received 14 layers with a near wall thickness of 0.2 [*mm*], and a total prism layer thickness of 50 [*mm*]. These refinement volumes are shown in Figure 3.

RANS Set-Up

Steady state RANS was used for simulations involving the opening angle sweep, the flap-endplate gap sweep, and the DRS actuator wake. Each of these simulations was ran on an 11 million cell polyhedral mesh, with the k-ω SST turbulence model, using the coupled solver within STAR-CCM+. Simulations were ran until force coefficients for downforce and drag dig not vary by more than 0.0005 over 400 iterations, this resulted in average residuals of 3.7E-3 for specific dissipation rate, 3.9E-5 for turbulent kinetic energy, 1.8E-5 for x-momentum, 6.3E-6 for y-momentum, 5.4E-6 for z-momentum, and 1.0E-7 for continuity.

FIGURE 4 Rear wing mesh cross-section

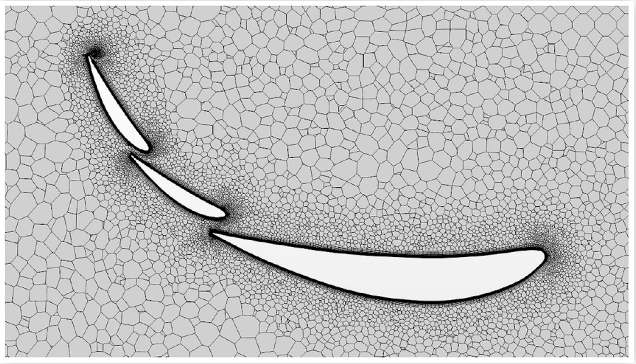

Flap Opening Angles For the simulations involving the rotation of the flaps, each flap was rotated about an axis at 70% of its cord along the mean camber line. Opening angles as high as 40° for flap 1 and 65° for flap 2 were simulated, with the baseline angles of attack being 32.5° for the first flap, and 57.5° for the second. An overlay of an open configuration and the closed configuration of the rear wing airfoils is shown in Figure 5, demonstrating the pivot point of the flaps.

Flap-Endplate Gap Flap-endplate gaps between 1 [*mm*] and 10 [*mm*] were modelled by the deletion of the flaps for the specified distance from the endplate. Mesh refinements were created in these gaps with a specified refinement size of 0.15 [*mm*], bringing the total mesh size to approximately 30 million cells, depending on the size of flap-endplate gap.

DRS Actuator The DRS actuator geometry being studied is a pneumatic cylinder mounted on the main plane of the rear wing, with a set of linkages and mounts connecting it to the flaps. While the pneumatic cylinder is mounted on the car centerline, the linkages are asymmetric, and would not be fully represented in any simulation using the real-world geometry. As such, the linkages were duplicated and mirrored about the centerline such that both of the linkages are represented, while this does result in more geometry being represented than the real-world, it provides for a conservative

FIGURE 5 Flap actuation range

FIGURE 6 Flap-endplate gap mesh closeup

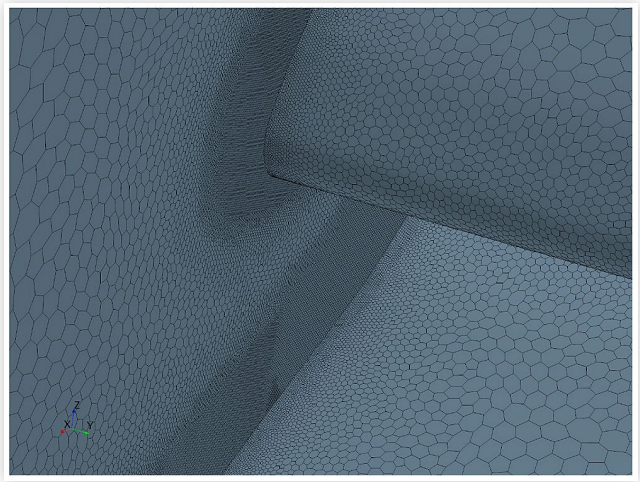

FIGURE 7 DRS Actuator Mirrored Geometry

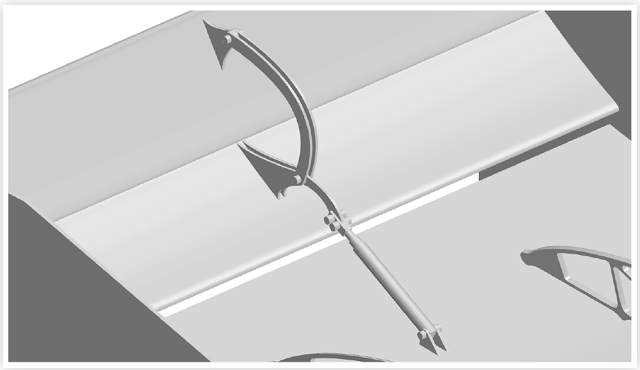

FIGURE 8 Flap overset mesh

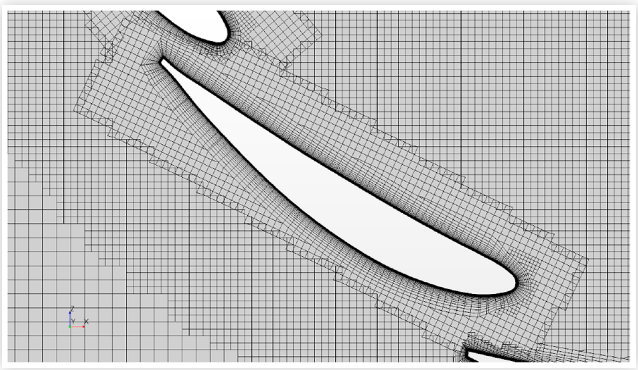

result. A 0.5 [*mm*] refinement was applied to the actuator surfaces in addition to a wake refinement extending 10 [*cm*] downstream, resulting in a mesh size of 22.1 million cells, an increase of 11.1 million cells relative to the baseline geometry.

Detached Eddy Simulation Set-Up

One difficulty faced by modern RANS turbulence models is the simulation of detached flows, with many models not being able to sufficiently predict the onset of flow separation [3]. Due to the lack of resources in the public domain on the simulation of DRS motion, the SST IDDES turbulence model was chosen to try and provide the most confident result within the computational budget. SST IDDES, short for Improved Delayed Detached Eddy Simulation using Menter's Shear Stress Transport model, is a hybrid RANS-LES model in which the near wall regions of the flow are using a traditional RANS turbulence model, with the rest of the flow to be simulated using Large Eddy Simulation (LES) as long as there is sufficient mesh resolution. This class of turbulence modeling has shown increased accuracy in the simulation of detached flows relative to URANS [3]. A 0.05 [*ms*] timestep was used to keep the convective CFL number under one throughout the majority of the domain. Meshing for this simulation was done using a hexahedral mesher. Five inner iterations were used for this simulation, resulting in average residuals of 1.6E-4 for the specific dissipation rate, 9.1E-6 for the x-momentum, 8.4E-6 for the y-momentum, 8.1E-6 for the z-momentum, 1.4E-7 for the turbulence kinetic energy, and 8.4E-8 for continuity.

Overset Mesh Motion In order to simulate the motion of the flaps, an overset mesh was used for each of the two flaps. The motion prescribed to the flaps was a linear profile from 25° and 50° to 0° for the first and second flaps respectively. This motion will occur over 50 [*ms*] as conservatively estimated from footage of TUG Racing's 2018 drag reduction system closing, as both systems use the same concept of a spring loaded pneumatic cylinder pivoting the flaps about a point far back on the mean camber line. Since the flaps have a passive closing mechanism, that being that the piston does not return by pressurized air, but rather a combination of a spring within the pneumatic cylinder in addition to the

FIGURE 9 DRS motion profile

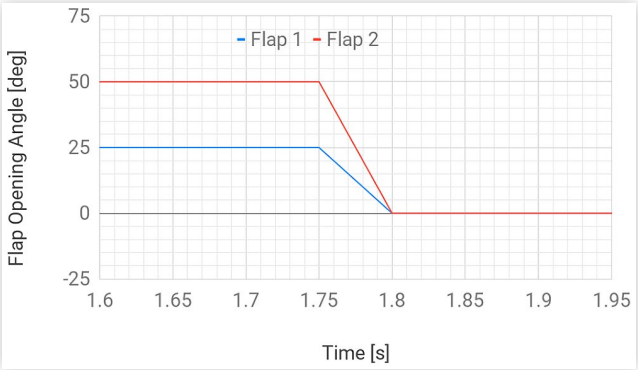

aerodynamic moment on the flaps naturally closes the system, a true closing time or motion profile cannot be determined without complex modeling or physical testing. Therefore, the results from this simulation are to be used as an initial insight into the dynamic behaviour of the system without being taken as a rigid claim of how these systems always behave.

Adapted Mesh Refinements Since suitable meshes for DES require a high level of resolution in order to reach sufficient accuracy, there is a motivation to make meshes that are efficient in having additional refinements where is required and nothing more. Due to the 'organic' nature of fluid flow, traditional refinement shapes such as cylinders and blocks often refine more of the fluid domain than is necessary, especially for complex flows such as open wheeled race cars. In an exploratory approach to solving this problem, a steady state RANS solution was found for the 'flaps closed' state of the car, which was used to create volumetric mesh refinements for the DES mesh. This was done through recommendations given by Addad et al. on relations between turbulence metrics and optimal unstructured mesh sizing for large eddy simulation:

"*The attempt of building an unstructured LES grid based on the Taylor microscale has been found very successful. However, as the Reynolds number is increased this sort of requirement might be excessive and eventually a criterion such as one tenth of the integral lengthscale could be sufficient*" [4]

As a function for a recommended mesh size h, this can be represented as:

$$h = max(\lambda, L) \tag{1}$$

Where the Taylor microscale, λ, and integral length scale, L, are calculated as:

$$h = \sqrt{\frac{10\nu k}{\epsilon}} \tag{2}$$

$$L = \frac{k^{3/2}}{\epsilon} \tag{3}$$

Using equation (1), threshold volumes can be created from a precursor solution at sizes of 10 [*mm*], 5 [*mm*], and 2.5 [*mm*], and used a volumetric refinements. After re-meshing and further solving of the RANS solution, this process was repeated again to result in 'smooth' volumetric refinements. Due to computational cost constrictions, these recommendations were not followed rigidly, but were still used for the creation of refinements as fine as 2.5 [*mm*] for the rear wing and 5 [*mm*] for the rest of the car. This resulted in a total mesh size of 55.4 million cells.

FIGURE 10 Recommended mesh sizing

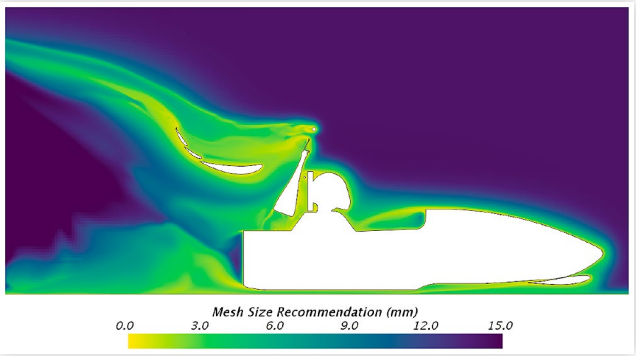

FIGURE 11 Adapted refinement, 5 [*mm*] sizing

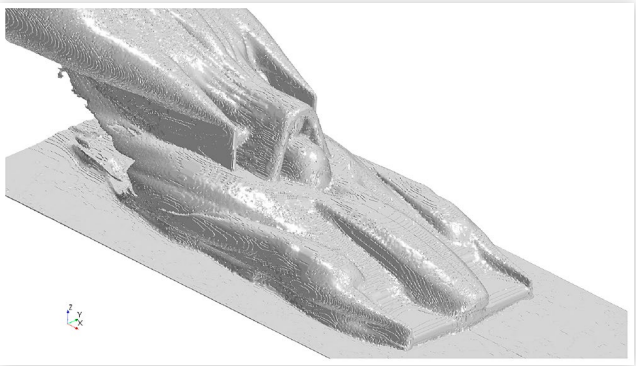

FIGURE 12 Adapted rear wing mesh

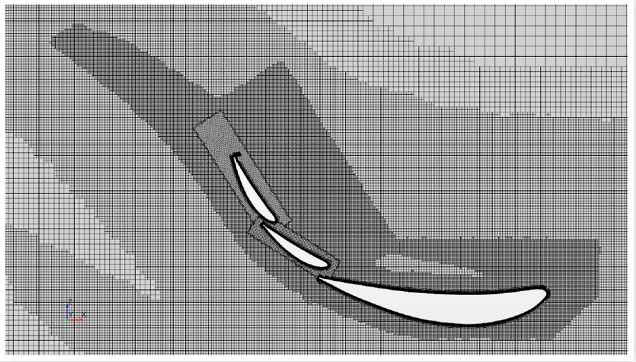

Results

Flap Opening Angles

A simulation sweep was done for the entire range of combinations of opening angles for the first and second flap, with a resolution of 5°. A total of 126 simulations were completed, with results for the relative rear wing drag, downforce, efficiency, and front aerodynamic balance being shown in Table 1, Table 2, Table 3, and Table 4 respectively. In order to aid in the filtering of configurations, the pitching moments about the pivot axis for flap 1 and flap 2 are considered, and are provided in Table 5 and Table 6 respectively.

For PBR20, positive pitching moments are required to close the flaps upon DRS deactivation, as the spring within the pneumatic piston is not strong enough for this task. As such, a negative moment at high speeds may overpower the spring and the mechanism will not begin to close at all. When looking at Table 5, it can be seen that flap 1 experiences negative closing moments at opening angles of 30 and over, with the opening of flap 2 also having a negative effect on the flap 1 closing moment as it is no longer able to 'drive' the flow behind flap 1.

When looking at Table 6, multiple strong patterns are observed. When the flap opening angles are equal ± 5°, the flap 2 closing moment is equivalent to, if not greater than the initial configuration. When flap 2 is opened less than flap 1, the flap 2 closing moment shows little influence from the opening angle of either flap. Finally, when flap 2 is opened more than flap 1, a strong decrease in the flap 2

TABLE 1 Drag relative to baseline [%]

Flap 2 Opening [deg] \ Flap 1 Opening [deg]	0	-5	-10	-15	-20	-25	-30	-35	-40
0	100	88	76	68	61	56	52	49	48
-5	93	82	70	63	57	53	49	47	46
-10	87	77	66	58	53	49	46	44	43
-15	80	72	63	54	50	45	43	41	40
-20	73	67	59	51	45	42	40	38	37
-25	66	61	55	48	42	37	36	35	34
-30	59	54	50	45	39	34	31	31	31
-35	52	48	44	40	35	31	28	27	28
-40	44	42	38	35	31	28	26	25	26
-45	36	33	32	29	27	24	22	22	24
-50	33	28	26	23	22	20	19	19	22
-55	35	30	25	21	18	16	15	16	18
-60	36	31	27	23	19	16	14	14	15
-65	37	33	29	24	21	17	15	14	16

TABLE 2 Downforce relative to baseline [%]

Flap 2 Opening [deg] \ Flap 1 Opening [deg]	0	-5	-10	-15	-20	-25	-30	-35	-40
0	100	91	82	75	68	62	57	53	48
-5	96	89	80	72	66	61	56	51	47
-10	94	87	80	71	65	60	54	50	45
-15	90	85	79	69	63	58	53	48	44
-20	87	83	78	70	61	55	50	46	42
-25	83	80	75	69	62	53	48	43	39
-30	77	75	71	67	61	54	47	41	37
-35	72	70	67	63	59	53	46	40	35
-40	65	64	61	58	54	50	45	39	36
-45	55	53	54	52	49	46	42	38	36
-50	50	45	44	42	42	40	37	35	35
-55	50	46	42	37	33	31	30	29	29
-60	49	45	41	37	33	28	23	21	21
-65	49	45	41	37	33	29	24	20	19

TABLE 3 Efficiency relative to baseline [%]

Flap 2 Opening [deg] \ Flap 1 Opening [deg]	0	-5	-10	-15	-20	-25	-30	-35	-40
0	100	104	108	110	112	111	111	107	101
-5	104	108	114	115	116	115	113	110	104
-10	108	113	121	121	121	121	118	114	105
-15	113	119	124	128	126	127	123	117	110
-20	118	123	132	136	136	132	127	122	113
-25	125	130	136	142	148	143	136	125	115
-30	131	137	143	150	157	158	151	132	119
-35	139	146	151	159	166	169	166	147	125
-40	147	153	161	167	175	179	175	158	135
-45	154	161	169	176	183	192	191	172	147
-50	152	160	171	182	191	203	198	180	160
-55	144	155	166	178	184	196	196	183	160
-60	138	146	155	163	175	178	169	154	137
-65	131	137	145	153	156	163	158	138	123

TABLE 4 Front aerodynamic balance

Flap 2 Opening [deg] \ Flap 1 Opening [deg]	0	-5	-10	-15	-20	-25	-30	-35	-40
0	41	45	49	52	56	59	62	65	67
-5	42	45	50	53	57	59	63	66	68
-10	44	47	51	54	58	61	64	67	69
-15	45	48	51	56	59	63	65	68	71
-20	48	49	51	56	61	64	67	70	72
-25	50	51	53	57	61	65	69	71	75
-30	53	54	56	58	61	66	70	74	77
-35	56	57	58	60	63	67	72	76	80
-40	60	61	62	64	66	68	72	76	79
-45	67	68	67	68	69	73	75	77	79
-50	70	73	75	75	75	77	79	80	81
-55	70	73	76	81	83	85	86	86	85
-60	70	73	77	79	84	88	92	95	95
-65	71	73	76	80	83	88	93	96	97

TABLE 5 Flap 1 closing moment relative to baseline [%]

Flap 2 Opening [deg] \ Flap 1 Opening [deg]	0	-5	-10	-15	-20	-25	-30	-35	-40
0	100	89	76	64	51	38	26	14	4
-5	96	86	73	60	48	35	22	10	-1
-10	92	82	70	56	44	31	18	5	-4
-15	88	79	67	51	39	26	12	0	-11
-20	83	75	64	47	33	20	7	-6	-17
-25	79	72	60	44	26	12	0	-12	-23
-30	74	67	57	42	23	4	-13	-20	-29
-35	70	63	54	40	21	1	-20	-33	-35
-40	65	59	51	37	21	1	-22	-40	-41
-45	58	53	47	36	20	1	-22	-41	-41
-50	56	49	43	33	20	2	-19	-36	-39
-55	56	50	43	32	20	4	-16	-31	-34
-60	55	50	43	34	22	6	-11	-25	-29
-65	54	49	44	35	23	9	-8	-22	-28

TABLE 6 Flap 2 closing moment relative to baseline [%]

Flap 2 Opening [deg] \ Flap 1 Opening [deg]	0	-5	-10	-15	-20	-25	-30	-35	-40
0	100	105	96	78	70	69	68	67	66
-5	96	106	97	73	69	68	67	66	66
-10	90	104	105	75	69	68	67	65	64
-15	82	101	110	88	71	67	66	64	64
-20	71	93	108	113	83	69	65	64	62
-25	55	76	97	113	113	84	67	62	60
-30	34	54	75	98	113	114	99	65	59
-35	14	31	50	73	97	113	115	96	64
-40	-11	4	22	43	67	93	111	114	92
-45	-34	-24	-9	11	33	57	85	108	91
-50	-40	-37	-33	-22	-4	19	45	70	77
-55	-45	-42	-39	-35	-30	-20	1	25	33
-60	-50	-48	-45	-41	-36	-31	-22	-13	-5
-65	-55	-53	-51	-48	-43	-38	-30	-21	-14

closing moment is observed as the angle of attack between the two flaps increases. In filtering the results based on the negative closing moments seen in these tables, Tables 1 through 4 are shown with a bold line separating the disallowed configurations. Table 7 shows the force coefficient for the overall closing moment of the system about flap 1, with disallowed configurations from this table being shown with parallel bold lines.

With the filtered results, Tables 1 through 3 may be used to determine the optimum configuration based on the criteria set by the team. When considering all simulations performed, a minimum drag of 13.6% was found at opening angles of 35° for flap 1 and 60° for flap 2. If the team is looking to minimize the drag or maximize the aerodynamic efficiency, an opening angle of 25° for flap 1 and 50° for flap 2 should be chosen. This configuration has an interesting standing within the results,

TABLE 7 Combined moment coefficient at flap 1 (C_m * A * 1E3), [m^2]

Flap 2 Opening [deg] \ Flap 1 Opening [deg]	0	-5	-10	-15	-20	-25	-30	-35	-40
0		11.6	10.0	8.3	6.6	5.0	3.4	1.8	0.6
-5		20.4	13.7	10.0	7.7	5.8	3.9	2.1	0.6
-10		28.8	18.3	11.7	8.7	6.4	4.3	2.3	0.9
-15		36.7	23.1	14.3	9.7	6.9	4.5	2.4	0.7
-20		42.1	27.1	19.3	11.5	7.5	4.8	2.3	0.5
-25		42.3	29.0	22.1	15.7	8.9	4.9	2.3	0.2
-30		37.1	27.1	22.5	17.8	12.5	6.9	2.3	0.0
-35		26.9	22.2	20.0	17.6	13.9	9.0	4.0	0.2
-40		10.8	14.1	14.8	14.3	13.0	10.0	6.1	2.6
-45		-11.8	2.4	7.5	9.0	9.0	8.2	6.8	3.6
-50		-25.7	-8.7	-2.1	1.8	3.5	4.0	4.0	3.3
-55		-33.5	-13.0	-6.9	-4.5	-3.2	-1.9	-0.7	-0.6
-60		-43.4	-18.0	-9.8	-6.5	-5.5	-5.4	-5.1	-4.5
-65		-53.3	-23.0	-13.4	-9.1	-7.4	-6.8	-6.3	-5.6

as it has both the minimum drag and downforce within all of the allowed configurations, the maximum aerodynamic efficiency within the entire data set, and is next to the transition line between positive closing moments and negative closing moments for each of the two flaps.

Further work would involve an second sweep around this configuration with higher resolution in flap opening angles to determine if these qualities always occur at the same point, or if they occur at similar but different points.

Flap-Endplate Gap Losses

A total of 10 flap-endplate gaps were simulated in addition to a zero-gap baseline case, with the results being shown in Figure 15. While a clean trend cannot be seen from the results, it can be seen that the existence of a flap-endplate gap only results in a minor performance loss, indicating that that the rear wing does not stall. Figure 13 shows a vector line integral convolution of the wall skin friction coefficient in vicinity of the flap-endplate gaps for the 2 [*mm*] case, and can be used to determine flow separation in this region. While no separation is observed, a streak of high skin friction coefficient with a large lateral component is observed. This streak can be attributed to a strong vortex created by the air leaking from the gap, as seen in Figure 14.

While the rear wing being simulated experienced tolerable losses from even large flap-endplate gaps of 10 [*mm*], it cannot be said that this will hold true for other multi element configurations. For example, a more aggressive rear wing could potentially experience aerodynamic stall from a similarly sized flap-endplate gap.

DRS Actuator Wake

Table 8 provides the absolute force coefficient for each rear wing component with and without the DRS actuator wake. The results show that the rear wing only experiences a 0.69% loss in downforce, and in-fact a 0.93% reduction in drag as well. An explanation for the drag reduction is that by the actuator wake reducing the total force produced by the wing, there comes enough of a reduction in induced drag to counteract any drag from the DRS actuator.

Detached Eddy Simulation - DRS Deactivation

The downforce, drag, and aerodynamic balance response of the vehicle to the DRS closing is shown in Figures 18, 19, and 20. Each plot shows a linear response, indicating that the flaps experience no leading edge separation or other breakdown in flow structure. An overshoot in lift, drag, and aerodynamic balance is seen at the starting and ending times of the DRS

FIGURE 13 Bottom view of flap 1 skin friction for 2 [*mm*] flap-endplate gap

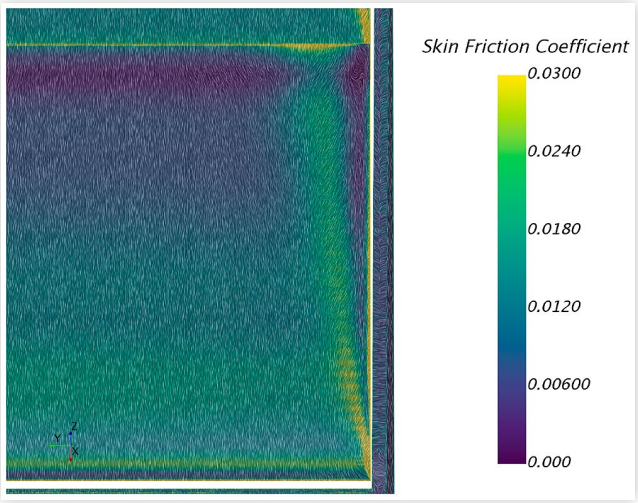

FIGURE 14 Lambda2 vortex criterion for 2 [*mm*] flap-endplate gap

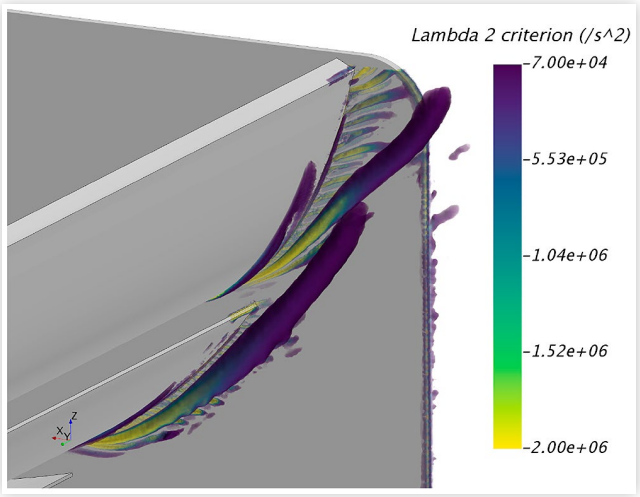

FIGURE 15 Relative aerodynamic performance versus flap-endplate gap width

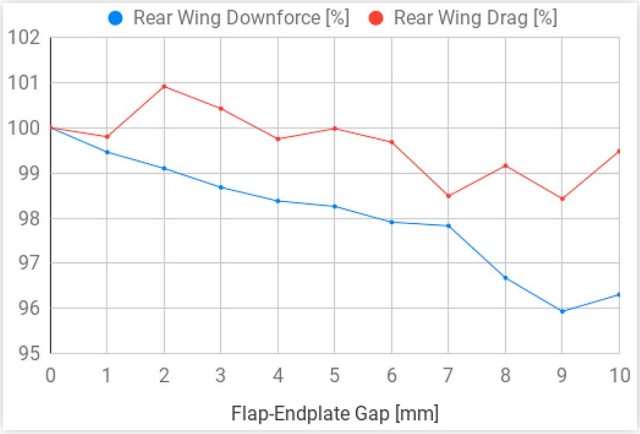

TABLE 8 Aerodynamic losses from DRS actuator wake

	C_L*A		C_D*A	
	No Linkage	Linkage	No Linkage	Linkage
Mainfoil	0.7687	0.7644 **(-0.56%)**	0.0699	0.0695 **(-0.57%)**
Flap 1	0.2739	0.2715 **(-0.88%)**	0.1604	0.1591 **(-0.81%)**
Flap 2	0.115	0.1134 **(-1.39%)**	0.1782	0.1755 **(-1.52%)**
DRS Linkage	n/a	0.0001	n/a	0.0006
Overall	1.1575	1.1495 **(-0.69%)**	0.4084	0.4046 **(-0.93%)**

FIGURE 16 Convective CFL number on symmetry plane

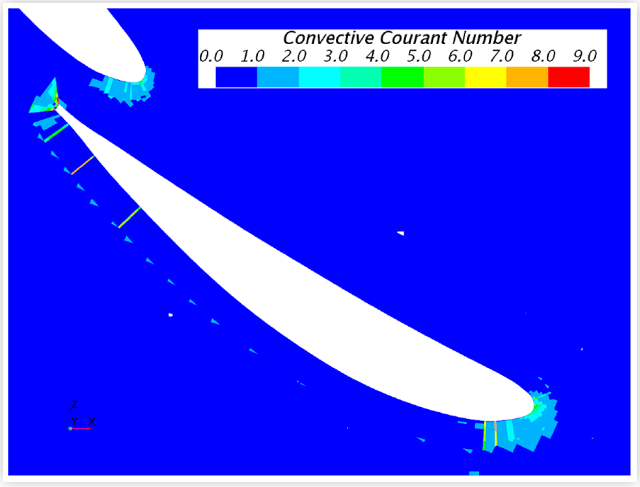

actuation, which can be attributed to the discontinuous velocity profile the flaps experience, resulting in infinite acceleration of the flaps at these times.

Due to the motion of the simulation geometry, time averaged statistics were not gathered for comparison to the stationary flap RANS solutions, and further simulation of the 'flaps closed' state of the car was not possible due to computational restrictions.

In examination of the convective CFL number along the symmetry plane, small groups of cells within the prism layers of the flaps had convective CFL numbers greater than 1. While this not ideal, the implicit second-order temporal scheme used does not have a strict requirement on convective CFL numbers. Since these areas of concern occur at the parts of the flap which leading edge separation would stem from (the primary concern for this simulation), simulations using smaller timesteps should be performed to ensure timestep independence has been reached.

FIGURE 17 Lambda2 vortex criterion ($\lambda_2 = 0$) before and after DRS actuation

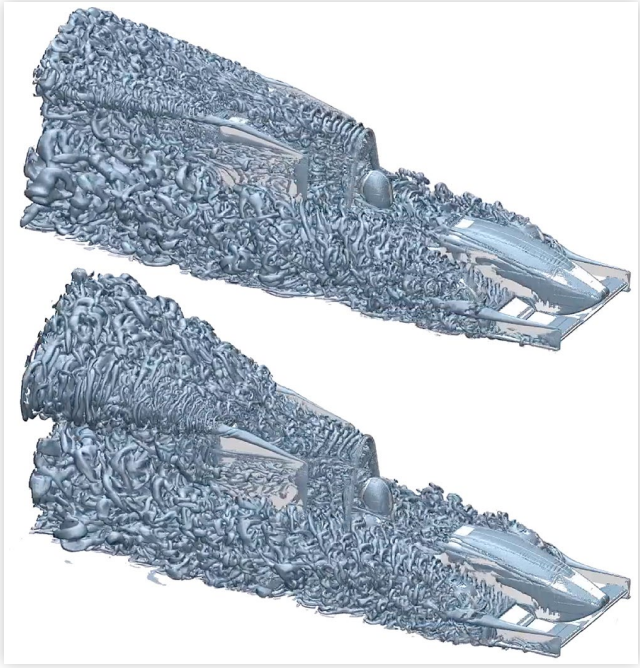

FIGURE 18 Downforce response to DRS closing

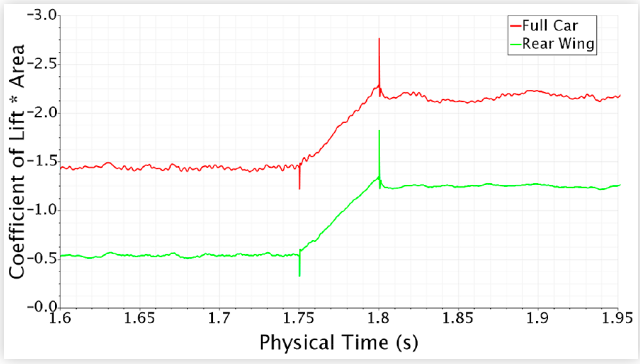

FIGURE 19 Drag response to DRS closing

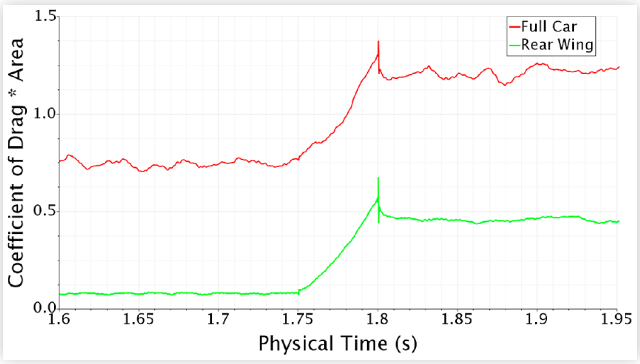

FIGURE 20 Front aerodynamic balance response to DRS closing

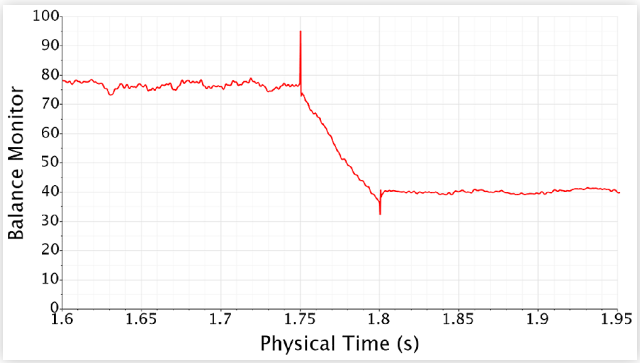

Conclusions

Multiple aerodynamic studies were performed on the University of Manitoba Formula SAE Team's PBR20 car with the aid of computational fluid dynamics. The design space defined by the opening angles of the first and second flap was characterised, with a single combination containing the minimum drag and minimum downforce within permittable opening angle combinations (determined by a positive closing moment), and maximum aerodynamic efficiency within all combinations. Losses in performance due to the existence of flap-endplate gaps and a DRS actuator wake were determined and found to be non-critical. Lastly, a detached eddy simulation using moving overset meshes was used to determine the dynamic behaviour of the drag reduction system upon closing, which was found to respond with the same linear profile prescribed to the flap motion.

References

1. Merkel, J.P., "Development of Multi-Element Active Aerodynamics for the Formula SAE Car," 54-60, 2013.
2. Siemens PLM, "Online Formula Student Training | MDX," 2019.
3. Ashton, N., West, A., Lardeau, S., and Revell, A., "Assessment of RANS and DES Methods for Realistic Automotive Models," *Computers and Fluids* 128:1-15, 2016.
4. Addad, Y., Gaitonde, U., Laurence, D., and Rolfo, S., "Optimal Unstructured Meshing for Large Eddy Simulations," *Quality and Reliability of Large Eddy Simulations* 93-103, 2008.

Contact Information

Please send any requests for further information to **David Penner** at David.Penner@mts.net

Acknowledgments

The author would like to acknowledge The University of Manitoba, SAE International, The University of Manitoba Student Chapter of SAE International (UMSAE), its advisors Ed Hohenberg and Dr. Paul Labossiere, the sponsors and donors of UMSAE, and the members of UMSAE Polar Bear Racing, all for their combined support and effort to make possible the learning experience that is Formula SAE. The author would also like to thank Siemens PLM for their sponsorship of STAR-CCM+ to UMSAE, fostering the advancement of CFD within engineering.

ISSN 0148-7191